

Energy-Efficient Dynamic Drive Control for Wind Power Conversion With PMSG: Modeling and Application of Transfer Function Analysis

Maren Kuschke and Kai Strunz

Abstract—A method for transfer function based modeling offering an in-depth insight into the systemic behavior of wind energy conversion systems (WECS) is developed. The originally nonlinear behavior of the drive system covering turbine, permanent magnet synchronous generator, and power electronic converter is rearranged and linearized resulting in a compact transfer function description. The locations of transfer function poles and zeros and related stability are readily identified as a function of WECS parameters and the operating point. Drive control design rules making use of the transfer functions for setting the compensation parameters depending on the wind speed are established. The behavioral differences between speed and power control loops can readily be appreciated. The synthesis of a power control loop to closely follow maximum available wind power is performed based on the design rules. In this context, the voltage sourced converter is operated in current mode control to contribute to fast adjustment of air-gap torque while maintaining currents within limits. The direct and quadrature current references are calculated to attain the desired torque at minimal stator current magnitude and so enhance energy efficiency. The dynamic performance of the design is evidenced by time-domain simulation and stochastic analysis.

Index Terms—Current mode control, electric drive, minimum-current-per-torque optimization, permanent magnet synchronous generator (PMSG), power control, power system, small-signal analysis, stability, transfer function, voltage sourced converter (VSC), wind energy.

I. INTRODUCTION

THE GLOBAL Wind Energy Council reported new wind power installation of 44,799 MW in 2012 [1]. The rising share of wind energy with its implications for power system operation calls for a profound understanding of the static and dynamic behavior and controls of wind energy conversion systems (WECS). Power electronic control adopts a key role in modifying the behavior of the different WECS technologies [2]–[8]. Examples for such control functions in normal operation include optimal power tracking under various conditions [9]–[14] or the smoothing of power fluctuations [15]–[19].

In the design of control architectures and the setting of compensation parameters for WECS, transients simulation and models for small-signal analysis are of interest. For wind

energy converters with permanent magnet synchronous generators (PMSG), linearization has been applied in the formulation of state-space representations to perform eigenvalue analysis and assess stability limits [20]–[24]. What is critically missing, however, are transfer function descriptions of the machine side that readily identify how all critical parameters of turbine, generator, and power electronic control impact dynamic behavior and stability. This is where the contributions of this paper come in. First, the machine side of a WECS is structured into the three functional stages of power synthesizer-controller, current vector optimizer-controller together with torque generation, as well as turbine-rotor interaction process. Within these functional stages, rigorous decompositions lead to well-defined blocks of power conversion and controls. For the PMSG, optimization is applied to yield minimal current amplitude and minimal resistive losses at a given air-gap torque. Second, compacted and illustrative transfer functions are formulated to readily identify associated poles and zeros pertaining to all functional stages. Such transfer functions have proven valuable in electric motor drive analysis [25]. A major difference here is the integration of the wind turbine characteristics. It will become clear how different wind speeds and rotor angular velocities affect dynamic performance and stability considering transfer function poles and zeros. Control parameter setting rules are developed for integral and lead-lag compensators. Third, a case study puts into evidence the validity and applicability of the proposed transfer functions and controller setting rules. While the descriptions focus on WECS with direct-drive PMSG and fully rated converters, the methods can also be readily adapted to WECS with gearbox or synchronous generators with electrical excitation [26].

Following this introduction, the overall model is considered in Section II. Transfer functions for the functional stage of current vector optimizer, controller, and torque generation are proposed in Section III. In Section IV, the nonlinear dynamic interaction of turbine and rotor is dealt with and linearized. Particular attention is attributed to the phase-lead behavior of the torque-to-power transfer function. The corresponding time constants are calculated as a function of WECS parameters and the operating point. Optimal power setting based on the shaft angular velocity is elaborated upon in Section V. The compacted and illustrative transfer functions of the power and speed control loops including mathematical expressions of the poles and zeros imposed by the turbine-rotor interaction process are developed in Section VI. Controller design

Manuscript received September 30, 2013; accepted October 30, 2013. Date of publication December 3, 2013; date of current version January 29, 2014. This work was supported by Reiner Lemoine Foundation. Recommended for publication by Associate Editor W. Gao.

The authors are with the Technische Universität Berlin, Berlin 10587, Germany (e-mail: maren.kuschke@ieee.org; kai.strunz@tu-berlin.de).

Digital Object Identifier 10.1109/JESTPE.2013.2293632

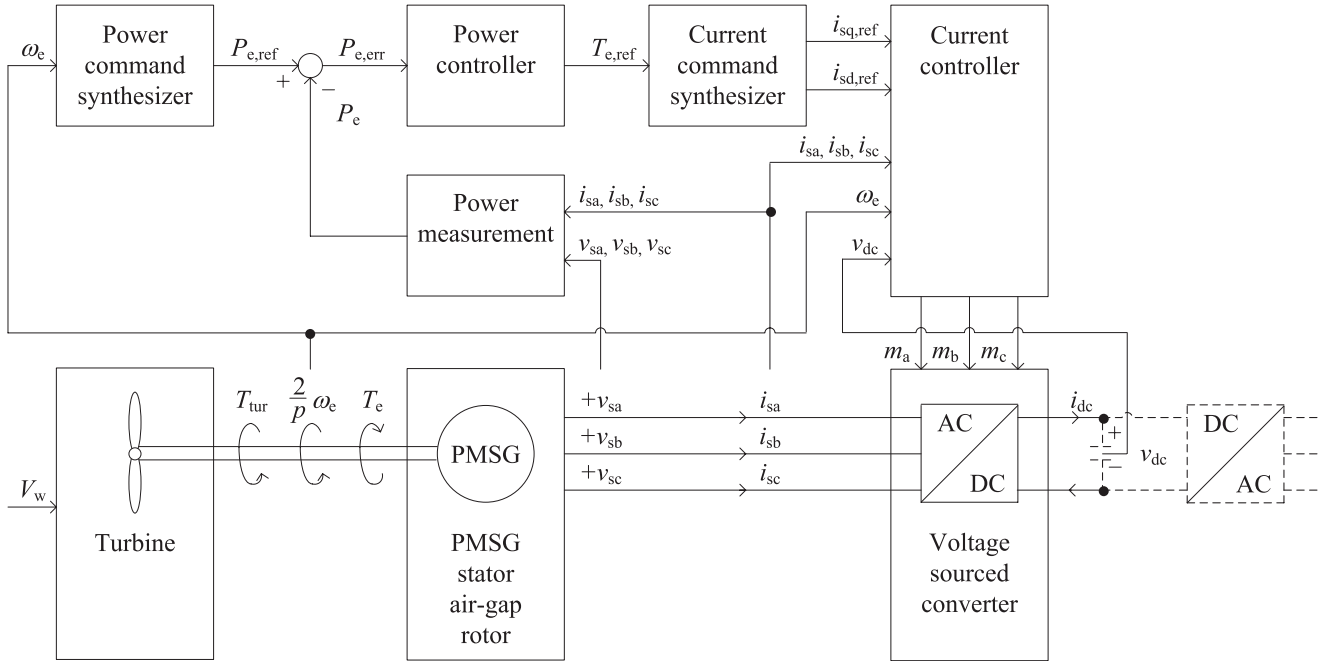


Fig. 1. Components and interactions of WECS using power control.

rules are derived, and the resulting performance is quantified through simulation and stochastic analysis in Section VII. Conclusion is drawn in Section VIII.

II. OVERALL BLOCK DIAGRAM

The drive system considered is the machine side of a WECS shown in Fig. 1. The wind at velocity V_w leads to an accelerating torque T_{tur} on the shaft through action of the turbine. The mechanical angular velocity of the rotor is equal to the electrical angular velocity ω_e $2 \times$ and divided by the number of poles p . The electromagnetic air-gap torque coming from the PMSG has a decelerating effect as the PMSG delivers electric power through the voltage sourced converter (VSC).

The direction and signs given for the three-phase stator voltages and currents shown between the blocks of PMSG and VSC follow the generator convention. Power delivered by the PMSG is counted positive in generator mode. On the dc side, the VSC is connected to a dc bus. Further resources may also be connected to the dc bus [27], [28]. A connection to the ac electric power grid is established through a dc-ac power electronic converter. The controls of this converter keep the dc voltage at the desired value. The control of this grid-connected converter is not described in this paper, and the interested reader is referred to [29] and [30].

The symbols m_a , m_b , and m_c at the output of the current controller denote the modulating signals that are compared with a PWM triangular carrier signal. The latter is assumed to have peaks at -1 and $+1$, and m_a , m_b , and m_c also lie within that range. A pulse width generator at the VSC generates switching pulses as for example shown in [29] and [30]. A current command synthesizer calculates the references for the current controller in the dq -domain [25]. The power controller in the outer control loop, shown on the top left of Fig. 1, in turn issues the torque reference that is then processed by the current command synthesizer. At the input of the power

controller, the measured power is compared with the power reference provided by the power command synthesizer. The latter sets the maximum available wind power based on the angular velocity of the rotor.

For the components depicted in Fig. 1, corresponding models are available in libraries of power electric or electronic system simulators. While these models are well suited for testing and analysis of behavior in the time domain, a more intuitive description of the system behavior is strongly desirable when it comes to the design of control loops. For this purpose, a description through a block diagram with transfer functions is helpful.

Fig. 2 shows a block diagram description derived from Fig. 1. The block diagram of Fig. 2 establishes the basis for the transfer function synthesis. The three-phase voltages and currents in the circuit have already been converted into dq -variables as a first step in this direction. This can readily be appreciated from the inputs and outputs of the PMSG. The latter is separated into three blocks pertaining to electrical, electromagnetic, and mechanical stages. In the following sections, the underlying equations will be rearranged to give a compact description and then linearized to allow for application of linear control theory and enhanced insight into system behavior of the drive. The sections follow the decomposition into three functional stages: 1) power synthesizer-controller; 2) current vector optimizer-controller and torque generation; and 3) turbine-rotor interaction process.

III. CURRENT VECTOR OPTIMIZER, CONTROLLER, AND TORQUE GENERATION

In this section, it is first reviewed how the electric system consisting of generator and VSC can be modeled by considering existing literature knowledge. It is discussed how a second-order closed current control loop representation based

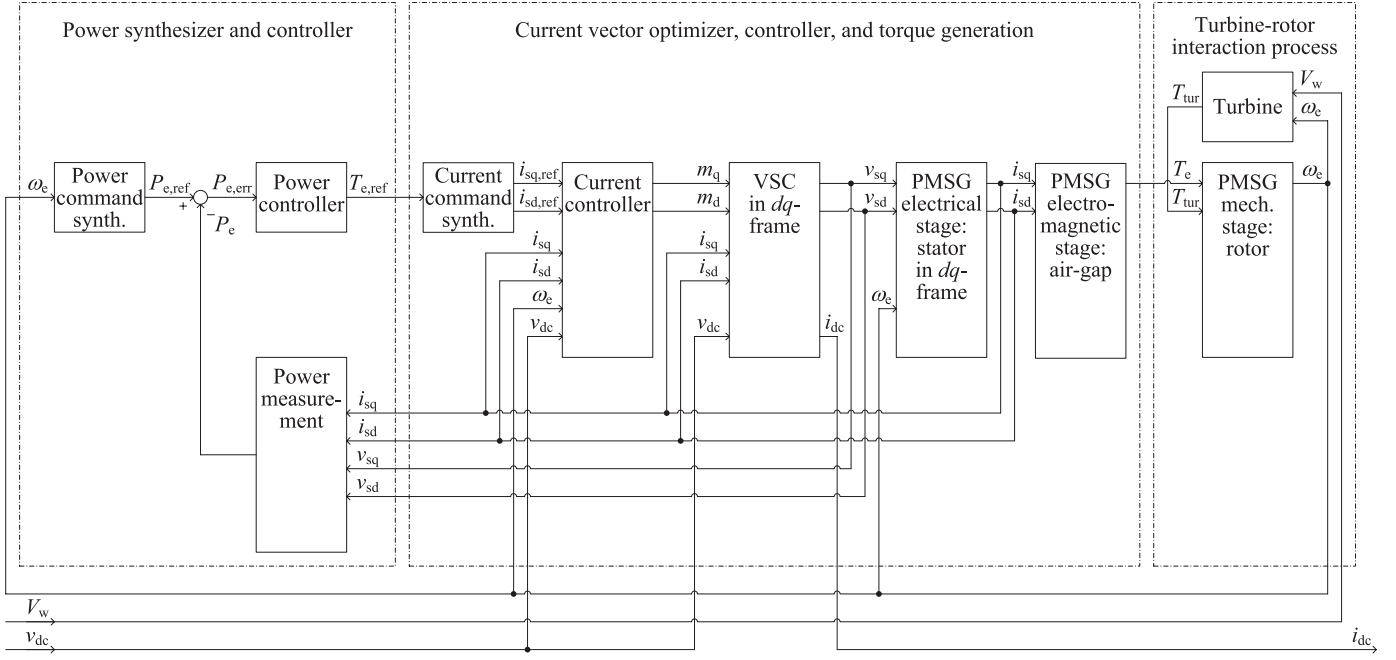


Fig. 2. Block diagram of WECS with functional stages framed by dashed lines.

on transfer functions is obtained. Then, a small-signal linearized formulation of the optimization for minimal stator current at a given torque is obtained.

A. Electric System Modeling

The stator equations are commonly expressed in a dq -frame that rotates at the electrical angular velocity ω_e of the rotor. The d -axis is magnetically centered on the north pole, and the q -axis leads the d -axis by 90° [31]. The generator mode convention with the direction of positive stator currents i_{sd} and i_{sq} out of the generator is applied

$$v_{sd} = L_{sq} i_{sq} \omega_e - L_{sd} \frac{di_{sd}}{dt} - R_s i_{sd} \quad (1)$$

$$v_{sq} = (\Phi_m - L_{sd} i_{sd}) \omega_e - L_{sq} \frac{di_{sq}}{dt} - R_s i_{sq} \quad (2)$$

where v_{sd} and v_{sq} are the d -axis and q -axis stator terminal voltages; L_{sd} and L_{sq} are the d -axis and q -axis stator inductances that are, respectively, composed of magnetizing and leakage inductances, Φ_m gives the amplitude of the magnetic flux linkage caused by the rotating permanent magnet in the stator, and R_s is the resistance of the stator phase windings.

The stator terminal voltages are obtained from the VSC and depend on the modulating signals and the dc voltage. On the dc side, the voltage is tapped to the reference node at the midpoint leading to a plus terminal $+(v_{dc}/2)$ and a minus terminal $-(v_{dc}/2)$. Considering the assumptions and further derivations of Appendix B, the VSC model is as follows:

$$v_{sd} = m_d \frac{v_{dc}}{2} \quad (3)$$

$$v_{sq} = m_q \frac{v_{dc}}{2} \quad (4)$$

$$i_{dc} = \frac{3}{4} (m_d i_{sd} + m_q i_{sq}) \quad (5)$$

B. Current Control Loop

The modulating signals m_d and m_q are produced by the current controller. Designing the current controller, it is important to understand the stator dynamics. For that purpose, (1) and (2) can be rewritten in the Laplace domain when neglecting initial conditions as

$$i_{sd} = -\frac{1}{R_s + sL_{sd}} (v_{sd} - L_{sq} i_{sq} \omega_e) \quad (6)$$

$$i_{sq} = -\frac{1}{R_s + sL_{sq}} (v_{sq} - (\Phi_m - L_{sd} i_{sd}) \omega_e) \quad (7)$$

Both equations are coupled. It is common practice to decouple the respective control loops by definition of substitute control variables

$$y_d = v_{sd} - L_{sq} i_{sq} \omega_e \quad (8)$$

$$y_q = v_{sq} - (\Phi_m - L_{sd} i_{sd}) \omega_e \quad (9)$$

These substitute control variables appear as outputs of the controller compensation functions $G_{i,d}(s)$ and $G_{i,q}(s)$. The latter have the current errors appear as inputs

$$y_d = G_{i,d}(s) (i_{sd,ref} - i_{sd}) \quad (10)$$

$$y_q = G_{i,q}(s) (i_{sq,ref} - i_{sq}) \quad (11)$$

The overall controller with outputs m_d , m_q is obtained from (10) and (11) by taking into account the decoupling terms imposed by (8), (9) and the equations (3), (4) pertaining to the VSC

$$m_d = \frac{2}{v_{dc}} (G_{i,d}(s) (i_{sd,ref} - i_{sd}) + L_{sq} i_{sq} \omega_e) \quad (12)$$

$$m_q = \frac{2}{v_{dc}} (G_{i,q}(s) (i_{sq,ref} - i_{sq}) + (\Phi_m - L_{sd} i_{sd}) \omega_e) \quad (13)$$

Fig. 17 in Appendix C illustrates the block diagram obtained so far. Inserting (8) into (6) and substituting y_d by (10) yields

after rearranging the closed loop transfer function for the d -axis

$$\frac{i_{sd}(s)}{i_{sd,ref}(s)} = \frac{-G_{i,d}(s)}{sL_{sd} + R_s - G_{i,d}(s)}. \quad (14)$$

For a proportional-integral (PI) compensator

$$G_{i,d}(s) = K_{d,P} + \frac{K_{d,I}}{s} \quad (15)$$

the closed loop function becomes

$$\frac{i_{sd}(s)}{i_{sd,ref}(s)} = \frac{-\frac{K_{d,P}}{L_{sd}} \left(s + \frac{K_{d,I}}{K_{d,P}} \right)}{s^2 + \left(\frac{R_s - K_{d,P}}{L_{sd}} \right) s - \frac{K_{d,I}}{L_{sd}}}. \quad (16)$$

The transient behavior of a first-order system can be obtained by applying pole-zero cancelation. **Canceling the pole of the stator circuit transfer function in (6) with the zero of the PI compensator (15) results in the condition**

$$\frac{K_{d,I}}{K_{d,P}} = \frac{R_s}{L_{sd}}. \quad (17)$$

Insertion into (16) yields

$$\frac{i_{sd}(s)}{i_{sd,ref}(s)} = \frac{1}{1 + s\tau_i} \quad (18)$$

with

$$\tau_i = -\frac{L_{sd}}{K_{d,P}}. \quad (19)$$

Applying PI compensator $G_{i,q}(s)$ and pole-zero compensation for the q -axis give likewise

$$\frac{K_{q,I}}{K_{q,P}} = \frac{R_s}{L_{sq}} \quad (20)$$

$$\frac{i_{sq}(s)}{i_{sq,ref}(s)} = \frac{1}{1 + s\tau_i} \quad (21)$$

$$\tau_i = -\frac{L_{sq}}{K_{q,P}}. \quad (22)$$

The **time constant τ_i readily defines the first-order responses** and **can be adjusted by setting $K_{d,P}$ and $K_{q,P}$** , respectively. Negative values are chosen to obtain positive time constants. A lower limit of τ_i is given by the requirement to damp noise as for example from power electronic switching. The possibility of obtaining a defined first-order dynamic behavior of the closed loop with time constant τ_i confirms the selection of the PI compensator type.

C. Air-Gap Torque

The electromagnetic torque generated in the air-gap of the PMSG is given by

$$T_e = \frac{3}{2} \frac{p}{2} (\Phi_m i_{sq} - (L_{sd} - L_{sq}) i_{sd} i_{sq}) \quad (23)$$

where T_e gives positive values for generator mode. Equation (23) represents the block of the PMSG electromagnetic stage in Fig. 2. For the purpose of small-signal analysis, (23) is linearized

$$\Delta T_e = \frac{3}{2} \frac{p}{2} (\Phi_m - (L_{sd} - L_{sq}) i_{sd}) \Delta i_{sq} - \frac{3}{2} \frac{p}{2} (L_{sd} - L_{sq}) i_{sq} \Delta i_{sd}. \quad (24)$$

D. Current Command Synthesizer

As shown in Fig. 2, the torque reference coming from the power controller is decomposed into current references by the current command synthesizer. **Based on a given reference for T_e , it is desirable to select the current vector references composed of $i_{sd,ref}$ and $i_{sq,ref}$ such that the magnitude $|i_s|$ is minimized.** This implies that the stator resistive losses are minimized and contributes so to the energy efficiency of the overall plant. As derived in Appendix D, the references can be obtained from the following equations:

$$i_{sd,ref} = \frac{-T_{e,ref}}{\frac{3}{2} \frac{p}{2} (L_{sd} - L_{sq}) i_{sq,ref}} + \frac{\Phi_m}{L_{sd} - L_{sq}} \quad (25)$$

$$i_{sq,ref}^4 + \frac{\Phi_m T_{e,ref}}{\frac{3}{2} \frac{p}{2} (L_{sd} - L_{sq})^2} i_{sq,ref} - \left(\frac{T_{e,ref}}{\frac{3}{2} \frac{p}{2} (L_{sd} - L_{sq})} \right)^2 = 0. \quad (26)$$

Such minimum-current-per-torque optimization is also known as maximum-torque-per-ampere in the literature on motor drive systems [25], and the solution for (26) is found iteratively. **It is further to be verified whether the solution of (25) and (26) leads to a stator rms voltage $|v_s| = (1/\sqrt{2})(v_{sq}^2 + v_{sd}^2)^{1/2}$ that stays within its maximum permissible limit.** For the small-signal analysis, this is assumed to be the case. **For small-signal analysis**, a linearization of (26) gives the following solution:

$$\Delta i_{sq,ref} = \frac{\frac{8}{3p} T_{e,ref} - \Phi_m i_{sq,ref}}{4i_{sq,ref}^3 \frac{3}{2} \frac{p}{2} (L_{sd} - L_{sq})^2 + \Phi_m T_{e,ref}} \Delta T_{e,ref}. \quad (27)$$

For the direct axis current, it follows from (25) that

$$\Delta i_{sd,ref} = \frac{T_{e,ref}}{\frac{3}{2} \frac{p}{2} (L_{sd} - L_{sq}) i_{sq,ref}^2} \Delta i_{sq,ref} - \frac{1}{\frac{3}{2} \frac{p}{2} (L_{sd} - L_{sq}) i_{sq,ref}} \Delta T_{e,ref}. \quad (28)$$

With (27) and (28), a linearization around the minimum-current-per-torque operating point is established. For the special case of $L_{sd} = L_{sq}$, it follows from (27) and (23) that

$$\Delta i_{sq,ref}|_{L_{sd}=L_{sq}} = \frac{4}{3p\Phi_m} \Delta T_{e,ref}. \quad (29)$$

Furthermore, for $L_{sd} = L_{sq}$, parameter $i_{sd,ref}$ would be set to zero.

E. Connection of Current Command Synthesizer, Current Control, and PMSG Electromagnetic Stage

The transfer functions (18) and (21) describing the closed-loop current control are linear and can so readily be applied in small-signal analysis. Adding the transfer functions (27) and (28) of the current vector optimizer and the transfer function (24) of the air-gap torque results in the block diagram of Fig. 3. When designing the outer power control loop, it is illustrative to bring the block diagram into the compact form shown in Fig. 4. This compacted form retains the dynamics of the current control loop but combines the algebraic relations from torque to currents and back to torque. This is sensible as these conversions do not lead to delays.

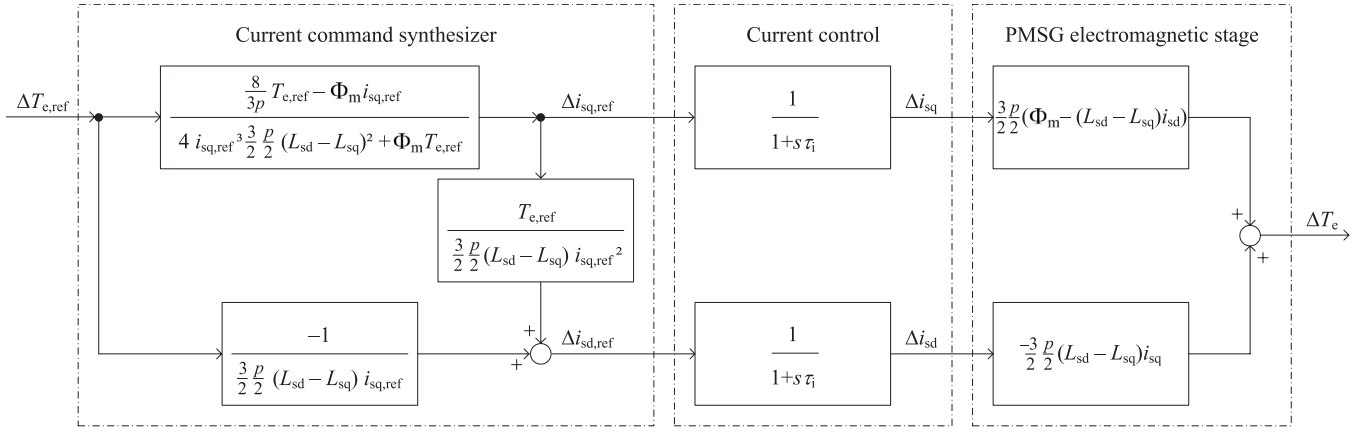


Fig. 3. Block diagram of current vector optimizer, compacted current control, and torque generation.

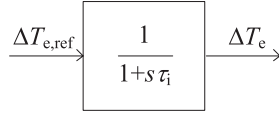


Fig. 4. Block diagram of compacted current vector optimizer, controller, and torque generation.

IV. TURBINE-ROTOR INTERACTION PROCESS

Assuming a rigid drive train, the equation of motion is given by

$$J \frac{2}{p} \frac{d\omega_e}{dt} = T_{\text{tur}} - T_e - T_d. \quad (30)$$

Here, p is the number of poles of the PMSG, and T_d can give damping due to friction. The aerodynamic torque T_{tur} of the wind turbine is given by

$$T_{\text{tur}} = \frac{1}{2} \pi \rho r^3 V_w^2 C_T(\lambda) \quad (31)$$

with the tip speed ratio

$$\lambda = \frac{\omega_m r}{V_w} \quad (32)$$

where ρ is the air density, r is the blade length, V_w is the wind velocity, ω_m is the mechanical angular velocity, and $C_T(\lambda)$ is the torque coefficient [6]. In Fig. 14 in Appendix A, a typical relation of $C_T(\lambda)$ is shown. Polynomials may be used to approximate the coefficient [32].

For limited excursions about a steady-state operating point, the torque coefficient may be approximated through a second-order polynomial

$$C_{T2} = c_0 + c_1 \lambda + c_2 \lambda^2. \quad (33)$$

Noting that mechanical and electrical rotor angular velocities are related by

$$\omega_m = \frac{2}{p} \omega_e. \quad (34)$$

The aerodynamic torque is approximated by inserting (32)–(34) into (31)

$$T_{\text{tur}} = \frac{1}{2} \pi \rho r^3 \left(c_0 V_w^2 + c_1 r \frac{2}{p} \omega_e V_w + c_2 r^2 \frac{4}{p^2} \omega_e^2 \right). \quad (35)$$

Linearization yields

$$\begin{aligned} \Delta T_{\text{tur}} = & \pi \rho r^3 \left(c_0 V_w + \frac{c_1 r \omega_e}{p} \right) \Delta V_w \\ & + \pi \rho r^3 \left(\frac{c_1 r V_w}{p} + \frac{4 c_2 r^2 \omega_e}{p^2} \right) \Delta \omega_e \end{aligned} \quad (36)$$

or

$$\Delta T_{\text{tur}} = (a_1 V_w + a_2 \omega_e) \Delta V_w + (a_2 V_w + a_3 \omega_e) \Delta \omega_e \quad (37)$$

with

$$a_1 = c_0 \pi \rho r^3, \quad a_2 = c_1 \frac{\pi \rho r^4}{p}, \quad a_3 = c_2 \frac{4 \pi \rho r^5}{p^2}. \quad (38)$$

The damping torque due to mechanical friction is

$$T_d = D \frac{2}{p} \omega_e. \quad (39)$$

The linearized version of (30) is obtained by considering small-signal deviations and (37)

$$\begin{aligned} \frac{d\Delta \omega_e}{dt} = & \frac{p}{2J} \left(a_2 V_w + a_3 \omega_e - D \frac{2}{p} \right) \Delta \omega_e \\ & + \frac{p}{2J} (a_1 V_w + a_2 \omega_e) \Delta V_w - \frac{p}{2J} \Delta T_e. \end{aligned} \quad (40)$$

Defining the mechanical lag time constant

$$\tau_\omega = - \frac{\frac{2J}{p}}{a_2 V_w + a_3 \omega_e - D \frac{2}{p}} \quad (41)$$

and applying the Laplace transform to (40) while neglecting initial conditions

$$\Delta \omega_e = - \frac{\frac{p}{2J} \tau_\omega}{1 + s \tau_\omega} \Delta T_e - \frac{\frac{a_1 V_w + a_2 \omega_e}{a_2 V_w + a_3 \omega_e - D \frac{2}{p}}}{1 + s \tau_\omega} \Delta V_w. \quad (42)$$

A block diagram interpretation of the transfer function is depicted in Fig. 5. The transfer function given by (42) is helpful for angular speed feedback control. For power control, however, power is needed as output. The electric power over the air-gap is obtained by multiplication of torque and speed

$$P_e = \frac{2}{p} T_e \omega_e. \quad (43)$$

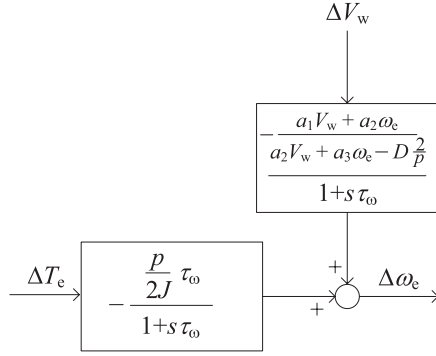


Fig. 5. Block diagram from air-gap torque and wind speed to angular velocity.

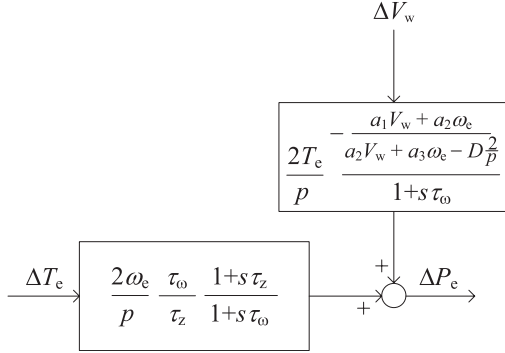


Fig. 6. Block diagram from air-gap torque and wind speed to air-gap power.

The linearized form is

$$\Delta P_e = \frac{2}{p} T_e \Delta \omega_e + \frac{2}{p} \omega_e \Delta T_e. \quad (44)$$

Inserting (42) into (44)

$$\Delta P_e = \left(-\frac{\tau_\omega T_e}{1 + s\tau_\omega} + \frac{2}{p} \omega_e \right) \Delta T_e - \frac{2}{p} T_e \frac{a_1 V_w + a_2 \omega_e}{a_2 V_w + a_3 \omega_e - D \frac{2}{p}} \Delta V_w. \quad (45)$$

Rearranging (45) gives

$$\Delta P_e = \frac{2}{p} \omega_e \frac{\left(1 - \frac{p\tau_\omega T_e}{2\omega_e J}\right) \left(1 + s \frac{\tau_\omega}{1 - \frac{p\tau_\omega T_e}{2\omega_e J}}\right)}{1 + s\tau_\omega} \Delta T_e - \frac{2}{p} T_e \frac{a_1 V_w + a_2 \omega_e}{a_2 V_w + a_3 \omega_e - D \frac{2}{p}} \Delta V_w. \quad (46)$$

Defining the lead time

$$\tau_z = \frac{\tau_\omega}{1 - \frac{p\tau_\omega T_e}{2\omega_e J}} \quad (47)$$

and insertion of (47) into (46) gives

$$\Delta P_e = \frac{2\omega_e \tau_\omega}{p\tau_z} \frac{1 + s\tau_z}{1 + s\tau_\omega} \Delta T_e - \frac{2T_e}{p} \frac{a_1 V_w + a_2 \omega_e}{a_2 V_w + a_3 \omega_e - D \frac{2}{p}} \Delta V_w. \quad (48)$$

The block diagram in Fig. 6 illustrates the transfer function. The phase-lead behavior in the path from ΔT_e to ΔP_e becomes clearly visible, and the magnitude of the phase-lead depends on the operating point. The phase-lead behavior was also observed experimentally in [23] and so confirms (48).

V. POWER SYNTHESIZER

For a given wind speed, the maximum power that can be extracted by a turbine is given by [4]

$$P_{\text{tur}} = \frac{1}{2} \pi \rho r^2 V_w^3 C_P(\lambda). \quad (49)$$

The power coefficient $C_P(\lambda)$ relates to torque coefficient $C_T(\lambda)$ by $C_P(\lambda) = C_T(\lambda)\lambda$ and reaches its maximum at λ_{opt} . With (32) and (34), (49) is expressed at λ_{opt} as the optimal regime curve

$$P_{\text{tur,opt}} = \frac{4}{p^3} \pi \rho r^5 \omega_e^3 \frac{C_P(\lambda_{\text{opt}})}{\lambda_{\text{opt}}^3}. \quad (50)$$

Neglecting the impact of mechanical power losses, this is the maximum power that can be transferred to the air-gap and is taken as a reference power of P_e (43) to support energy efficiency

$$P_{e,\text{ref}} = P_{\text{tur,opt}}. \quad (51)$$

Angular velocity ω_e is the only time-varying quantity that $P_{\text{tur,opt}}$ depends on at $\lambda = \lambda_{\text{opt}}$. Function (50) is used to give the optimal power reference in the power command synthesizer in Fig. 2. It allows for following the maximum power in the wind at partial load and fixed pitch when the maximum rotational speed has not been reached.

The reference is compared with the measured electric power, and the difference is fed to the power controller. The power delivered over the terminal of the PMSG is calculated from the terminal currents and voltages

$$P_{\text{ter}} = \frac{3}{2} (v_{sd} i_{sd} + v_{sq} i_{sq}). \quad (52)$$

Inserting (1) and (2) gives

$$P_{\text{ter}} = \frac{3}{2} (\omega_e \Phi_m i_{sq} + \omega_e (L_{sq} - L_{sd}) i_{sd} i_{sq}) - \frac{3}{2} \left(R_s (i_{sd}^2 + i_{sq}^2) + L_{sd} i_{sd} i_{sd} + L_{sq} i_{sq} i_{sq} \right). \quad (53)$$

With (43), (23) and the following definitions, (53) can be decomposed as

$$P_{\text{ter}} = P_e - P_R - P_L \quad (54)$$

with

$$P_R = \frac{3}{2} R_s (i_{sd}^2 + i_{sq}^2) \quad (55)$$

$$P_L = \frac{3}{2} (L_{sd} i_{sd} i_{sd} + L_{sq} i_{sq} i_{sq}). \quad (56)$$

Power P_R gives the resistive losses in the PMSG stator windings. Power P_L is positive when the magnetic energy stored in the stator inductances is increased. This power P_L is only nonzero during transients when currents i_{sd} and i_{sq} change. Losses P_R have been minimized by the minimum-current-per-torque optimization described in Section III. The contributions of P_R (55) and P_L (56) in (54) can be used to better approximate P_e

$$P_e = P_{\text{ter}} + P_R + P_L. \quad (57)$$

The power measurement as depicted in Fig. 2 is then representative of the air-gap power (43).

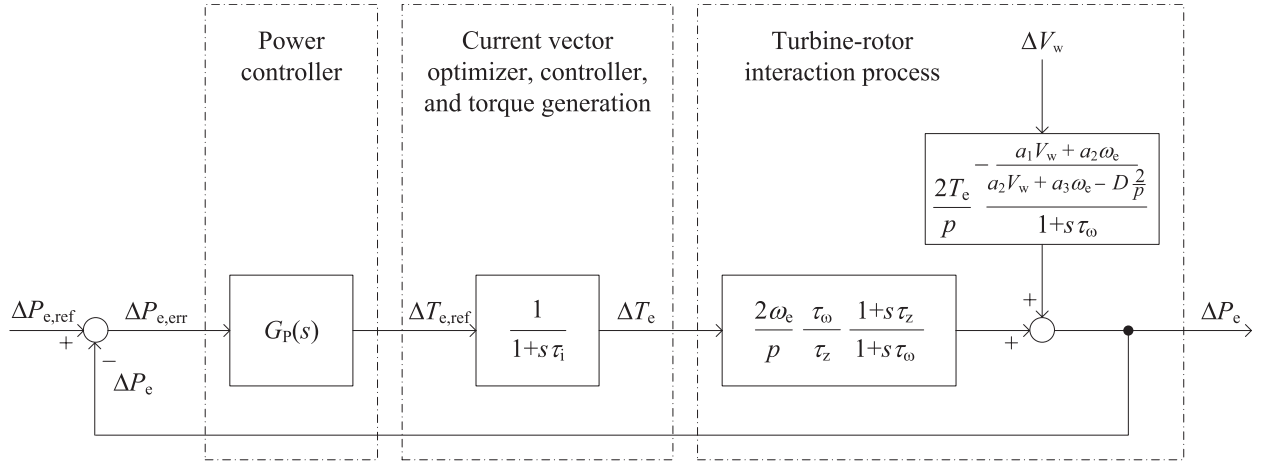


Fig. 7. Block diagram of compacted linearized power control loop.

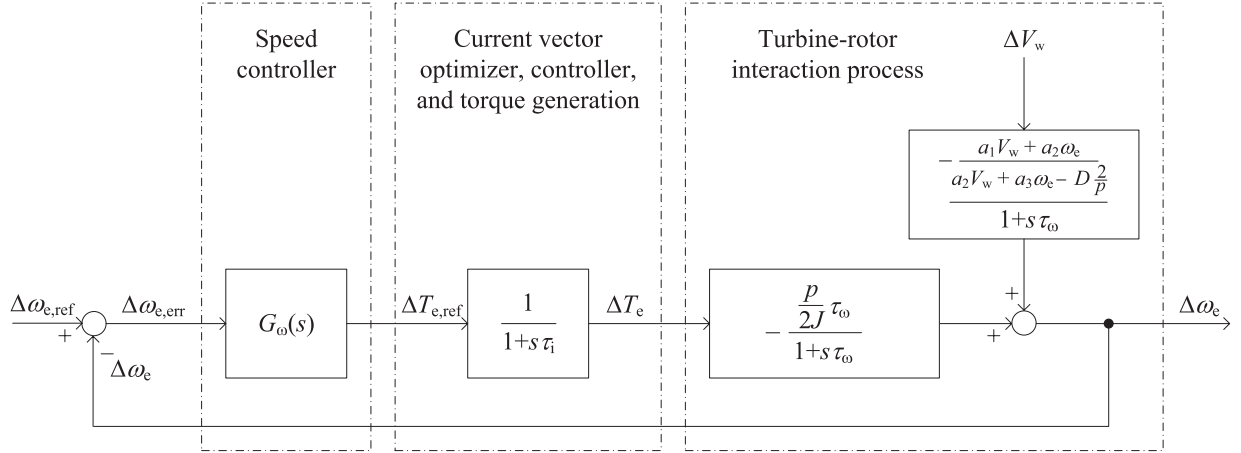


Fig. 8. Block diagram of compacted linearized speed control loop.

VI. COMPACT LOOP FOR STABILITY ANALYSIS AND CONTROLLER DESIGN

Considering Figs. 2, 4, and 6, the compact form of the power control loop in Fig. 7 is obtained. Through the derivations described in Sections III and IV, the original block diagram of Fig. 2 has now been brought into a format that lends itself to the design of the power controller aimed at following the optimal regime curve at fixed pitch. Likewise, using Fig. 5, the compact form of a speed control loop to give a desired angular velocity is obtained. The block diagram is shown in Fig. 8. This loop may serve as an alternative to the power control loop depending on preferences. In that case, following maximum power can be realized by measuring the wind velocity and then calculating the reference $\omega_{e,\text{ref}}$ for the given optimal tip speed ratio λ_{opt} using (32) and (34). Both block diagrams are representative of the key phenomena of dynamic behavior of power and angular velocity expected on the synchronous generator side of WECS. At the same time, the transfer functions are compact and illustrative.

The designs of the inner current control loops for d -axis and q -axis as well as the current vector optimization have been elaborated upon in Section III, and so also define the time constant τ_i . The latter is several orders of magnitude smaller than the time constant τ_ω , which defines the time it

takes for rotor accelerations or decelerations in response to steps of torque.

The definition of τ_ω through (41) illustrates its dependence on the operating point. In fact, τ_ω can become negative and so lead to a positive pole, respectively, eigenvalue $s_\omega = -1/\tau_\omega$ and instability of the turbine-rotor interaction process. Such regions of instability occur on the rising slope of C_T on the left of its peak in Fig. 14 when a positive change of angular speed ω_e leads to acceleration as given by (40). For tracking the maximum power (50), the operating point is to the right of the peak of C_T at the falling slope. There, s_ω is negative and is a dominant pole in the uncompensated system. Time constant τ_z also depends on the operating point. For $\tau_\omega > 0$: $\tau_z > 0$ if $\omega_m > \tau_\omega T_e/J > 0$. Equation (47) also shows that then $\tau_z > \tau_\omega$.

The phase-lead behavior from ΔT_e to ΔP_e in the power control loop can also be appreciated from (45). A change in ΔT_e is instantaneously fed forward with gain $2/p \cdot \omega_e$ leading to a step change of air-gap power ΔP_e . Then, an exponential decay of the latter follows according to the change of the angular speed toward the new steady state at $\Delta P_e = (2\omega_e/p) (\tau_\omega/\tau_z) \Delta T_e$. The phase-lead behavior from ΔT_e to ΔP_e dominates the response of the open loop in Fig. 7 as τ_i is comparatively small.

VII. STUDY FOR CONTROLLER DESIGN, LARGE-SIGNAL ANALYSIS, AND SIMULATION

In what follows, the value of the developed framework of transfer functions is put into evidence by a case study that is comprised of two major stages. At first, rules for establishing a possible power controller are established. Then, the design is verified through simulation of the large-scale nonlinear model of Fig. 1 implemented in MATLAB/Simulink. A stochastic analysis of tracking maximum available wind power is performed.

A. Controller Design

The block diagrams of the compacted linearized control loops of Section VI are well suited for the design of controllers. In the turbine-rotor interaction process of the power control loop, it is assumed that $\tau_\omega > 0$, $\tau_z > 0$. The integral plus lead-lag compensator $G_P(s)$ proposed for this loop is of the following format:

$$G_P(s) = \frac{K}{s} \frac{1 + s\tau_{le}}{1 + s\tau_{lg}}. \quad (58)$$

The lag and lead time constants τ_{lg} and τ_{le} are introduced to compensate the process behavior due to τ_z and τ_ω . As the process is stable, pole-zero cancelation can be performed. The process pole is compensated by choosing

$$\tau_{le} = \tau_\omega \quad (59)$$

the process zero is compensated by setting

$$\tau_{lg} = \tau_z. \quad (60)$$

The remaining parameter K is set by direct consideration of the closed-loop transfer function of Fig. 7 given that pole-zero cancelation has been applied as mentioned above

$$\frac{\Delta P_e(s)}{\Delta P_{e,ref}(s)} = \frac{1}{1 + s \frac{p\tau_z}{K2\omega_e\tau_\omega} + s^2 \frac{\tau_i p\tau_z}{K2\omega_e\tau_\omega}}. \quad (61)$$

Neglecting the small time constant τ_i , it can be seen that then the second-order behavior effectively reduces to first-order behavior with a pole at $s_{PI} = -K(2\omega_e/p)(\tau_\omega/\tau_z)$. The time constant of the closed loop can then be approximated by

$$\tau_{PI} = \frac{1}{K} \frac{p}{2\omega_e} \frac{\tau_z}{\tau_\omega}. \quad (62)$$

A larger value of K will enhance dynamic power tracking, but the sensitivity toward improving the speed in the response of the angular velocity $\Delta\omega_e$ is relatively low. On the other hand, too large a K can stress the generator shaft. The setting of K is inversely proportional to the desired τ_{PI}

$$K = \frac{1}{\tau_{PI}} \frac{p}{2\omega_e} \frac{\tau_z}{\tau_\omega}. \quad (63)$$

As an example, the data representative of a 3 MW turbine and the operating point in the Appendix A are considered. The parameters of the current control were set to give $\tau_i = 2$ ms. The closed-loop time constant is set to $\tau_{PI} = 0.05\tau_\omega$ with $\tau_\omega = 11.5$ s. The design of the controller was tested by means of a step of $\Delta P_{e,ref} = -50$ kW down from the operating point giving maximal power tracking, which was obtained for a tip

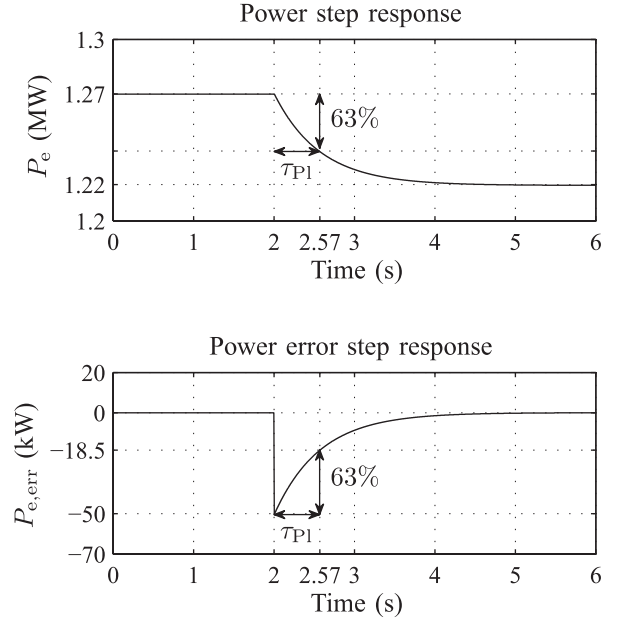


Fig. 9. Response to step of -50 kW of electric power in full nonlinear model.

speed ratio $\lambda_{opt} = 7$ and a wind speed of $V_w = 9$ m/s. The simulation was run using the large-scale nonlinear model of Fig. 1 with the power command synthesizer replaced by a step function generator. The result in Fig. 9 shows that the design made based on the compacted linearized power control loop of Fig. 7 yields a step response in the nonlinear model as expected from the setting of τ_{PI} . This is clear evidence of the valid approximation given by the developed linearization.

The controller design rules have been established for a particular operating point. When the average wind speed changes, the dynamic performance can be enhanced by adapting the compensation parameters. For example, it can be seen from Fig. 6 that the gain of the process is proportional to ω_e and so increases for a given λ_{opt} with higher wind speeds. Thus, there will be less control effort necessary at higher ω_e and wind speeds.

B. Large-Signal Analysis and Simulation

The validation of the design in following the maximum power points is made for a wind speed varying around an average of 9 m/s. The Von Kármán spectrum is used and a turbulence intensity of 0.16 considered as specified in the IEC standard [33]. The wind turbulence is generated by a shaping filter fed with white noise [34]. The controller design is implemented in the large-signal nonlinear model with blocks as described in Fig. 2. The switching frequency of the VSC model is at 5 kHz. The overall model includes the power reference $P_{e,ref}$ given by (50).

A 120-s window of results over time is displayed in Fig. 10. The wind speed series is depicted on the top. This is followed by the air-gap torque, the stator current q -axis and d -axis components. Both components contribute to the development of the air-gap torque as evidenced by (23). The results show how the current vector optimizer described in Section III-D

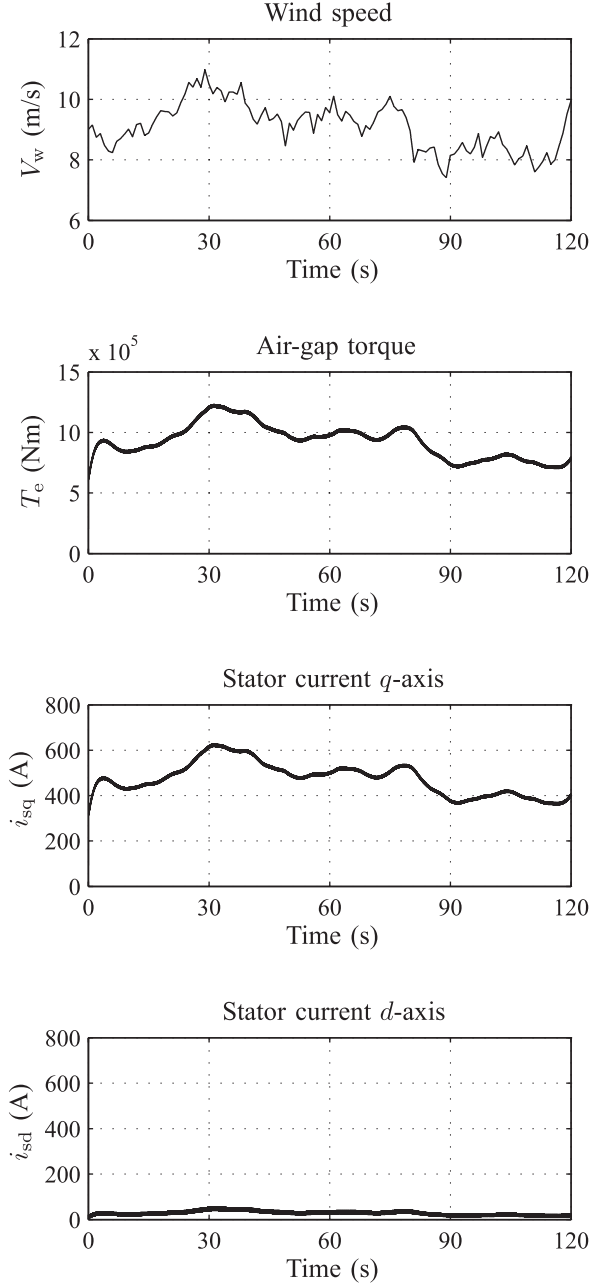


Fig. 10. Time series of wind speed over 2 min, air-gap torque, and stator current d -axis and q -axis components in full nonlinear model.

decomposes the stator current into i_{sq} and i_{sd} . To minimize losses for a given torque, (25) and (26) have been solved and programmed into a lookup-table for fast online access.

To perform a stochastic analysis, the window of simulation was extended from 120 s as above to 10 min as depicted in Fig. 11. The tracking of the optimal power curve at partial load (49) over this 10-min interval is assessed in the left graph of Fig. 12. It shows that the trajectories closely follow the optimal regime. The optimal regime is indicated by the dashed curve, which is mostly covered by the trajectories around it. The stochastic analysis of the results leads to the power error distribution quantifying the error made while tracking.

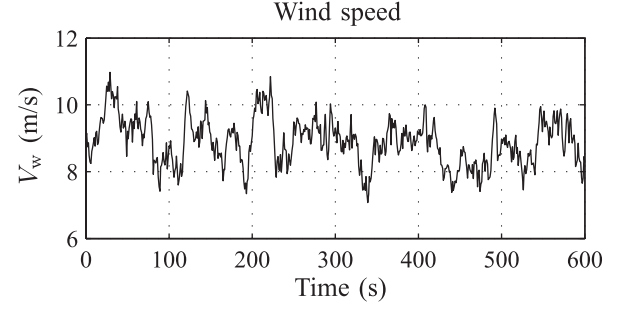


Fig. 11. Time series of wind speed over 10 min.

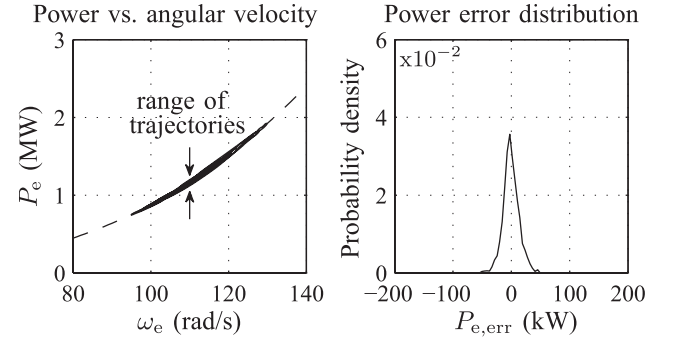


Fig. 12. Large-signal wind turbulence response power tracking.

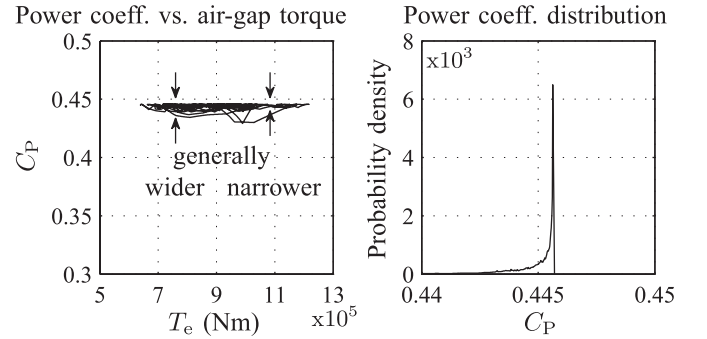


Fig. 13. Large-signal wind turbulence response power coefficient tracking.

The outcome depicted on the right confirms that the optimal power curve is being followed closely. The error could be further reduced by increasing K in (58).

In Fig. 13 on the left, the power coefficient C_p is plotted versus the air-gap torque for the same interval of 10 min. The narrow range within which the maximum $C_{p,opt}$ is being tracked is well observed by the distribution on the right. A closer look at the C_p versus T_e plot reveals that around $T_e = 10 \cdot 10^5 \text{ N}\cdot\text{m}$ the range of C_p is generally narrower than at the lower $T_e = 8 \cdot 10^5 \text{ N}\cdot\text{m}$. This observation is consistent with the statement made in the previous Section VII-A saying that the gain of the process rises with the wind speed. Tracking is so improved at higher wind speeds for the same compensator settings.

The results obtained for the large-scale simulation with the nonlinear model confirm the system insight obtained and

substantiate the drive control system design using the transfer functions based on the linearization. The parameter selection for the compensator has shown to yield good tracking of optimal operating points for wind power harvesting in the presence of significant wind turbulence. At the same time, the stator losses were minimized through a minimum-current-per-torque scheme.

VIII. CONCLUSION

A methodology for modeling the ensemble of wind turbine, PMSG, and VSC in the form of transfer functions that lend themselves to stability analysis and control system design was developed. The transfer functions for designing power and speed control loops are compact, but at the same time are illustrative in showing the system impact on dynamic behavior and stability. The influence of the operating point on the locations of WECS transfer function poles and zeros can be appreciated. The methodology serves as a framework for selecting compensator functions and tuning their parameters.

The overall methodology is distinguished by three contributions. First, the machine-side WECS was structured into block diagram format clearly identifying the various stages of power conversion and control. Linearization was applied to support small-signal analysis across all stages. It was shown how the phase-lead transfer function relating torque and power is influenced by wind speed and angular velocity of the rotor. The VSC connected to the generator is operated in current-mode control. A small-signal description of the minimum-current-per-torque optimization was developed and employed for the case that generator d -axis and q -axis inductances are unequal. Second, the transfer functions have been arranged into a compact format such that they provide an intuitive framework for control system design. Locations of poles and zeros and stability are identified, and an integral plus lead-lag compensator is designed for power control. The established design rules readily allow for adaptive compensator tuning depending on the operating point. This was evidenced by the design of the drive control system for energy efficiency. The control tracks maximum available wind power dynamically while at the same time decomposing the stator current into direct and quadrature axis components for loss minimization. Third, large-signal time-domain simulation was performed to verify the design. A stochastic analysis leading to the distributions of power coefficient and deviation of the power from its maximum confirmed a close following of maximum power setpoint.

In sum, the contributions made offer a better and enhanced insight into the various parameters influencing the behavior of wind energy conversion involving PMSG. This again has shown to be a valuable basis for compensator tuning making effective use of power electronics to control wind power converters for energy efficiency. Future work would extend the modeling to further physical phenomena such as the torsional movement of flexible shafts and consider other controls.

TABLE I
WIND TURBINE PARAMETERS

| Symbol | Quantity | Value |
|-----------------|--------------------------------------|--------|
| P_{tur} | Rated power | 3 MW |
| V_w | Rated wind speed | 12 m/s |
| n | Rated rotor speed | 18 rpm |
| $C_{P,opt}$ | Maximum power coefficient | 0.446 |
| r | Rotor radius | 45 m |
| λ_{opt} | Optimal tip speed ratio | 7 |
| H | Inertia constant of turbine and PMSG | 5 s |

TABLE II
PMSG PARAMETERS

| Symbol | Quantity | Value |
|----------|-----------------------------|---------------|
| p | Number of poles | 160 |
| R_s | Stator resistance | 50 m Ω |
| L_{sd} | Stator d -axis inductance | 4 mH |
| L_{sq} | Stator q -axis inductance | 6 mH |
| Φ_m | Flux induced by magnets | 16.2 Wb |

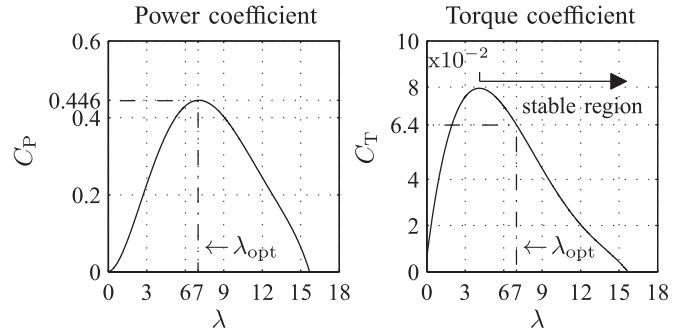


Fig. 14. Power coefficient $C_P(\lambda)$ and torque coefficient $C_T(\lambda)$.

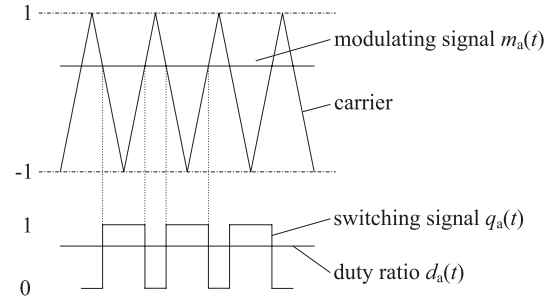


Fig. 15. Relations of modulation, switching, and duty ratio.

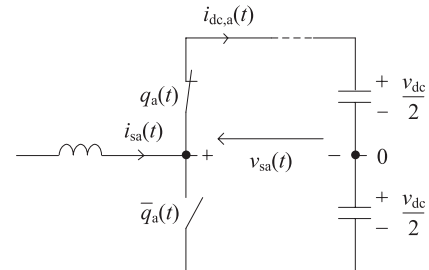


Fig. 16. Switch status representation of phase a of two-level three-phase VSC.

APPENDIX

A. Example Data

The following data refers to the WECS studied in Section VII. Wind turbine parameters are given in Table I,

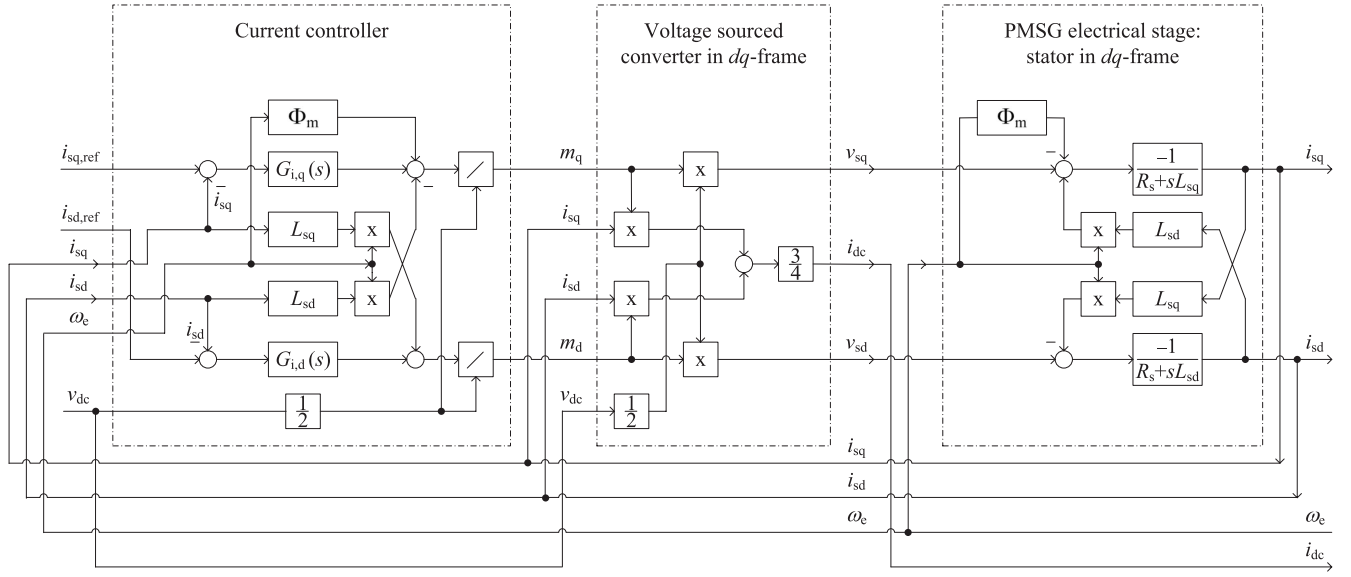


Fig. 17. Block diagram of current control.

relevant PMSG parameters are summarized in Table II. Power and torque coefficients as a function of tip speed ratio are depicted in Fig. 14. Both coefficients are related by

$$C_T(\lambda) = C_P(\lambda)/\lambda. \quad (64)$$

Damping due to mechanical friction was neglected. The following parameters are valid for the operating point of the simulation at $V_w = 9$ m/s: $P_{\text{tur}} = 1.27$ MW, $n = 13.5$ rpm, and $T_e = 8.95 \cdot 10^5$ N·m.

Coefficients for the second-order polynomial approximating the C_T curve around the operating point at $\lambda = 7$ as stated in (33): $c_0 = 2.25 \cdot 10^{-2}$, $c_1 = 2.18 \cdot 10^{-2}$, and $c_2 = -0.23 \cdot 10^{-2}$. The current control parameters are set such that $\tau_i = 2$ ms. The dc voltage is $v_{dc} = 6$ kV.

B. Details on VSC Average Modeling in dq-Domain

As mentioned in Section II, it is assumed here that the VSC is controlled by a sine-triangle PWM involving modulating sine signals m_a , m_b , and m_c that are compared with a triangular carrier ranging between -1 and $+1$. Other assumptions are possible, but would lead to variations of the average model.

The used PWM modulation scheme is illustrated in Fig. 15. The duty ratio $d_a(t)$ is the average of the switching signal $q_a(t)$. Modulating signals $m_a(t)$ and $d_a(t)$ are related by

$$d_a(t) = \frac{(1 + m_a(t))}{2}. \quad (65)$$

The switching signals are supplied to the switches, for which the leg of phase a is shown in Fig. 16. When $q_a = 1$, then the instantaneous voltage of v_{sa} is $+(v_{dc}/2)$, and when $q_a = 0$, then it is $-(v_{dc}/2)$. Therefore, the following average representation holds:

$$v_{sa} = d_a \frac{v_{dc}}{2} + (1 - d_a) \left(-\frac{v_{dc}}{2} \right). \quad (66)$$

Insertion of (65) yields

$$v_{sa} = m_a \frac{v_{dc}}{2}. \quad (67)$$

Applying the dq -transform, (3) and (4) are readily obtained. The average dc current is obtained by summing up the average currents on the dc side of each phase leg

$$i_{dc} = d_a i_{sa} + d_b i_{sb} + d_c i_{sc}. \quad (68)$$

Inserting (65)

$$\begin{aligned} i_{dc}(t) &= \left(\frac{1 + m_a(t)}{2} \right) i_{sa}(t) + \left(\frac{1 + m_b(t)}{2} \right) i_{sb}(t) \\ &+ \left(\frac{1 + m_c(t)}{2} \right) i_{sc}(t) = \frac{1}{2} (i_{sa}(t) + i_{sb}(t) + i_{sc}(t)) \\ &+ \frac{1}{2} (m_a(t) i_{sa}(t) + m_b(t) i_{sb}(t) + m_c(t) i_{sc}(t)). \end{aligned} \quad (69)$$

In a balanced three-phase system $i_{sa} + i_{sb} + i_{sc} = 0$, which is assumed here. Applying the dq -transform gives (5).

VSC losses may be neglected as the latter are small and not of key relevance when it comes to the dynamic behavior of the VSC. If needed, losses may be accounted for by adding resistance in series with the already represented stator resistance.

C. Current Control Loop

Fig. 17 offers an illustrative description of (3)–(7), (12), and (13).

D. Details on Current Command Synthesizer

Assuming that the references $i_{sq,\text{ref}}$ and $T_{e,\text{ref}}$ are known, then insertion of those references into (23) allows for calculating $i_{sd,\text{ref}}$. This then leads to (25).

The stator resistive losses are proportional to the square of the rms stator current $|i_s|^2 = 1/2(i_{sd}^2 + i_{sq}^2)$. Using (25) to eliminate i_{sd} in (55) gives

$$P_R = \frac{3}{2} R_s \left(i_{sq}^2 + \left(\frac{-T_{e,\text{ref}}}{\frac{3}{2} \frac{p}{2} (L_{sd} - L_{sq}) i_{sq}} + \frac{\Phi_m}{L_{sd} - L_{sq}} \right)^2 \right). \quad (70)$$

For the given $T_{e,ref}$ in (70), the resistive power losses P_R are minimized for $dP_R/di_{sq} = 0$. The solution is $i_{sq,ref}$ and found by solving (26).

REFERENCES

- [1] Global Wind Energy Council, Brussels, Belgium. (2012). *Global Wind Report* [Online]. Available: <http://www.gwec.net>
- [2] F. Blaabjerg and K. Ma, "Future on power electronics for wind turbine systems," *IEEE J. Emerg. Sel. Topics Power Electron.*, vol. 1, no. 3, pp. 139–152, Sep. 2013.
- [3] M. Liserre, R. Cardenas, M. Molinas, and J. Rodriguez, "Overview of multi-MW wind turbines and wind parks," *IEEE Trans. Ind. Electron.*, vol. 58, no. 4, pp. 1081–1095, Apr. 2011.
- [4] M. G. Simoes and F. A. Farret, *Alternative Energy Systems: Design and Analysis with Induction Generators*. Cleveland, OH, USA: CRC Press, 2008.
- [5] H. Polinder, F. F. A. an der Pijl, G.-J. de Vilder, and P. J. Tavner, "Comparison of direct-drive and geared generator concepts for wind turbines," *IEEE Trans. Energy Convers.*, vol. 21, no. 3, pp. 725–733, Sep. 2006.
- [6] J. F. Manwell, J. G. McGowan, and A. L. Rogers, *Wind Energy Explained*. New York, NY, USA: Wiley, 2002.
- [7] A. Yazdani and R. Iravani, "A neutral-point clamped converter system for direct-drive variable-speed wind power unit," *IEEE Trans. Energy Convers.*, vol. 21, no. 2, pp. 596–607, Jun. 2006.
- [8] R. Cardenas, R. Pena, G. Tobar, J. Clare, P. Wheeler, and G. Asher, "Stability analysis of a wind energy conversion system based on a doubly fed induction generator fed by a matrix converter," *IEEE Trans. Ind. Electron.*, vol. 56, no. 10, pp. 4194–4206, Oct. 2009.
- [9] K. Tan and S. Islam, "Optimum control strategies in energy conversion of PMSG wind turbine system without mechanical sensors," *IEEE Trans. Energy Convers.*, vol. 19, no. 2, pp. 392–399, Jun. 2004.
- [10] M. Chinchilla, S. Arnaltes, and J. C. Burgos, "Control of permanent-magnet generators applied to variable-speed wind-energy systems connected to the grid," *IEEE Trans. Energy Convers.*, vol. 21, no. 1, pp. 130–135, Mar. 2006.
- [11] C. Evangelista, P. Puleston, F. Valenciaga, and L. M. Fridman, "Lyapunov-designed super-twisting sliding mode control for wind energy conversion optimization," *IEEE Trans. Ind. Electron.*, vol. 60, no. 2, pp. 538–545, Feb. 2013.
- [12] R. G. de Almeida, E. D. Castronuovo, and J. A. Pecas Lopes, "Optimum generation control in wind parks when carrying out system operator requests," *IEEE Trans. Power Syst.*, vol. 21, no. 2, pp. 718–725, May 2006.
- [13] F. D. Kanellos and N. D. Hatziaargyriou, "Optimal control of variable speed wind turbines in islanded mode of operation," *IEEE Trans. Energy Convers.*, vol. 25, no. 4, pp. 1142–1151, Jun. 2010.
- [14] Y. Xia, K. H. Ahmed, and B. W. Williams, "New maximum power point tracking technique for permanent magnet synchronous generator based wind energy conversion system," *IEEE Trans. Power Electron.*, vol. 26, no. 12, pp. 3609–3620, Dec. 2011.
- [15] M. E. Haque, M. Negnevitsky, and K. M. Muttaqi, "A novel control strategy for a variable wind turbine with a permanent-magnet synchronous generator," *IEEE Trans. Ind. Appl.*, vol. 46, no. 1, pp. 331–339, Jan./Feb. 2010.
- [16] C. Luo, H. Banakar, B. Shen, and B.-T. Ooi, "Strategies to smooth wind power fluctuations of wind turbine generator," *IEEE Trans. Energy Convers.*, vol. 22, no. 2, pp. 341–349, Jun. 2007.
- [17] J. Lin, Y. Sun, Y. Song, W. Gao, and P. Sorensen, "Wind power fluctuation smoothing controller based on risk assessment of grid frequency deviation in an isolated system," *IEEE Trans. Sustain. Energy*, vol. 4, no. 2, pp. 379–392, Apr. 2013.
- [18] A. Uehara, A. Pratap, T. Goya, T. Senjyu, A. Yona, N. Urasaki, et al., "A coordinated control method to smooth wind power fluctuations of a PMSG-based WECS," *IEEE Trans. Energy Convers.*, vol. 26, no. 2, pp. 550–558, Jun. 2011.
- [19] C. Abbey, K. Strunz, and G. Joos, "A knowledge-based approach for control of two-level energy storage for wind energy systems," *IEEE Trans. Energy Convers.*, vol. 24, no. 2, pp. 539–547, Jun. 2009.
- [20] H. Geng and D. Xu, "Stability analysis and improvements for variable-speed multipole permanent magnet synchronous generator-based wind energy conversion system," *IEEE Trans. Sustain. Energy*, vol. 2, no. 4, pp. 459–467, Oct. 2011.
- [21] H. Huang, C. Mao, J. Lu, and D. Wang, "Small-signal modelling and analysis of wind turbine with direct drive permanent magnet synchronous generator connected to power grid," *IET Renew. Power Generat.*, vol. 6, no. 1, pp. 48–58, Feb. 2012.
- [22] N. P. W. Strachan and D. Jovicic, "Stability of a variable-speed permanent magnet wind generator with weak AC grids," *IEEE Trans. Power Delivery*, vol. 25, no. 4, pp. 2779–2788, Oct. 2010.
- [23] J. Munteanu, A. J. Bratcu, N.-A. Cutululis, and E. Ceanga, *Optimal Control of Wind Energy Systems*. New York, NY, USA: Springer-Verlag, 2008.
- [24] O. Alizadeh and A. Yazdani, "A strategy for real power control in a direct-drive PMSG-based wind energy conversion system," *IEEE Trans. Power Delivery*, vol. 28, no. 3, pp. 1297–1305, Jul. 2013.
- [25] P. Krause, O. Wasynczuk, and S. Sudhoff, *Analysis of Electric Machinery and Drive Systems*. New York, NY, USA: Wiley, 2002.
- [26] H. Polinder, J. A. Ferreira, B. B. Jensen, A. B. Abrahamsen, K. Atallah, and R. A. McMahon, "Trends in wind turbine generator systems," *IEEE J. Emerging Sel. Topics Power Electron.*, vol. 1, no. 3, pp. 174–185, Sep. 2013.
- [27] H. Louie and K. Strunz, "Superconducting magnetic energy storage (SMES) for energy cache control in modular distributed hydrogen-electric energy storage systems," *IEEE Trans. Appl. Supercond.*, vol. 17, no. 2, pp. 2361–2364, Jun. 2007.
- [28] K. Strunz and E. K. Brock, "Stochastic energy source access management: Infrastructure-integrative modular plant for sustainable hydrogen-electric co-generation," *Int. J. Hydrogen*, vol. 31, no. 9, pp. 1129–1141, Aug. 2006.
- [29] N. Mohan, T. Undeland, and W. Robbins, *Power Electronics: Converters, Applications and Design*. New York, NY, USA: Wiley, 2003.
- [30] A. Yazdani and R. Iravani, *Voltage-Sourced Converters in Power Systems*. New York, NY, USA: Wiley, 2010.
- [31] P. Kundur, *Power System Stability and Control*. New York, NY, USA: McGraw-Hill, 2003.
- [32] M. G. Simoes, B. K. Bose, and R. J. Spiegel, "Fuzzy logic based intelligent control of a variable speed cage machine wind generation system," *IEEE Trans. Power Electron.*, vol. 12, no. 1, pp. 87–95, Jan. 1997.
- [33] Int. Electrotech. Commission, Geneva, Switzerland, Tech. Rep. IEC 61400-1, 2005.
- [34] C. Nichita, D. Luca, B. Dakyo, and E. Ceanga, "Large band simulation of the wind speed for real time wind turbine simulators," *IEEE Trans. Energy Convers.*, vol. 17, no. 4, pp. 523–529, Dec. 2002.



Maren Kuschke received the Dipl.-Ing. degree from Technische Universität (TU) Berlin, Berlin, Germany, in 2008. She studied electrical engineering with focus on electrical drives, photovoltaics, and electric energy systems at TU Berlin and KTH Stockholm, Sweden.

Her work is supported by the Reiner Lemoine Foundation. Her current research interests include tidal energy conversion systems and power grid control.

Maren Kuschke received the VDI Award from the Association of German Engineers in 2009 and the IEEE PES German Chapter Best Master Thesis Award in 2010.



Kai Strunz received the Dipl.-Ing. and Dr.-Ing. degrees (*summa cum laude*) from the Saarland University, Saarbrücken, Germany, in 1996 and 2001, respectively.

He was with Brunel University, London, U.K., from 1995 to 1997. From 1997 to 2002, he was with the Division Recherche et Développement of Electricité de France, Paris, France. From 2002 to 2007, he was an Assistant Professor of electrical engineering with the University of Washington, Seattle, WA, USA. Since 2007, he has been Professor for Sustainable Electric Networks and Sources of Energy (SENSE) at Technische Universität (TU) Berlin, Berlin, Germany.

Dr. Strunz was the Chairman of the Conference IEEE PES Innovative Smart Grid Technologies, TU Berlin, in 2012. He is a Chairman of the IEEE Power and Energy Society Subcommittee on Distributed Generation and Energy Storage and Vice Chairman of the Subcommittee on Research in Education. On behalf of the Intergovernmental Panel on Climate Change, he acted as a Review Editor for the Special Report on Renewable Energy Sources and Climate Change Mitigation.